In Situ Electrochemical Monitoring of the Crevice Corrosion Process of the 7075-T651 Aluminium Alloy in Acidic NaCl and NaNO$_3$ Solution

Shengjie Wang [1,2], **Yamin Cao** [3,*], **Xiaohang Liu** [4] **and Guangyi Cai** [1,2,*]

1 National Key Laboratory of Science and Technology on Electromagnetic Energy, Naval University of Engineering, Wuhan 430033, China
2 East Lake Laboratory, Wuhan 420202, China
3 Marine Equipment Inspection & Testing Co., Ltd., Qingdao 266200, China
4 Goertek Optical Technology Co., Ltd., Weifang 261041, China
* Correspondence: caoyamin1004@163.com (Y.C.); caiguangyi@hust.edu.cn (G.C.)

Abstract: The crevice corrosion of the 7075-T651 aluminium alloy was investigated using in situ electrochemical impedance spectroscopy (EIS), potentiodynamic polarization curves (PC), and H$^+$ sensors in acidic NaCl solution with different contents of NaNO$_3$. In the solution without NaNO$_3$, the pH in the crevice increased rapidly and gradually reached a relatively stable status. The corrosion of the aluminium alloy in the crevice was inhibited and crevice corrosion could not be initiated. In the solution with NaNO$_3$, the pH increased rapidly at the initial immersion period and then decreased gradually. The corrosion of the aluminium alloy inside the crevice could be enhanced and the corrosion of the aluminium alloy outside crevice could be inhibited. This triggered crevice corrosion in the solution with NaNO$_3$. The inhibited corrosion outside the crevice can be attributed to the improved passive film of the specimen outside the crevice by nitrate. The accumulated secondary products of ammonia inside the crevice led to selective dissolution of copper, which triggered the nucleation of pitting corrosion and promoted the corrosion of the specimen inside the crevice.

Keywords: crevice corrosion; pH sensors; electrochemical monitoring; high strength aluminium alloy

1. Introduction

High-strength aluminium alloys, with high strength and low density, are among the most important materials for conveyance to achieve lightweight, and it has been widely applied in the transportation industry. However, high-strength aluminium alloys are vulnerable to localized attack in corrosion media containing chloride ions [1–4]. An aluminium alloy is more susceptible to localized corrosion (namely crevice corrosion) when its surface is covered with crevice structures such as rivets, lap joints, and thread connections [5–7]. Crevice corrosion is initiated due to the change in the composition of the solution inside the crevice. It has been reported that a concentration difference in metal ions [8], dissolved oxygen [9], H$^+$, and Cl$^-$ [10,11] could be formed. This leads to the macro separation of anode and cathode, and then drives the active dissolution of metal inside crevice. Once crevice corrosion is initiated, serious localized defects could be formed in a relatively short period. The strength of materials decreases drastically after the occurrence of crevice corrosion. This poses a significant threat to the service life of high-strength aluminium alloy components.

Various attempts have been made to inhibit the corrosion of aluminium and its alloys [12–16]. It has been reported that NO$_3^-$ can be considered an effective inhibitor for aluminium and its alloys. Li et al. [15] reported that NaNO$_3$ promoted the formation of thick oxide films on AA1085 and then re-passivated the pitting corrosion. Gao et al. [17] found that NaNO$_3$ significantly improved the properties of an oxide film, and the localized

attack was completely inhibited when the concentration of $NaNO_3$ was above 0.03 M. However, the role of NO_3^- on the corrosion of aluminium alloys is still controversial. Balaskas et al. [18] observed that a low concentration of NO_3^- inhibited the corrosion of the 2024 aluminium alloy, but was susceptible to localized attack at a high concentration of NO_3^-. The deterioration of the inhibiting properties at high concentrations was attributed to the presence of the NO_3^- ions that promoted the redeposition of copper at the cathodic sites. Blanc et al. [19] proposed that NH_3 could selectively dissolve copper and induce pitting nucleation due to the reduction of NO_3^-. The concentration of NO_3^- inside the crevice decreased gradually due to the reduction reaction and the limited diffusion process when the crevice was formed on the aluminium alloy surface. This improved the performance of a passive film inside the crevice and outside the crevice. However, the secondary product NH_3 progressively accumulated in the crevice solution, which affected the corrosion of the aluminium alloy inside the crevice. This indicated that the effect of NO_3^- on the corrosion of the aluminium alloy inside the crevice was different from that outside the crevice in a corrosive medium. Thus, it is essential to ascertain the effect of NO_3^- on crevice corrosion of high-strength aluminium alloys.

In this study, the crevice corrosion behaviour of the 7075-T651 aluminium alloy in an acidic NaCl solution with various concentrations of $NaNO_3$ was systematically studied. The corrosion behaviour and comparison of the aluminium alloy inside and outside the crevice was analysed using electrochemical measurements and surface analysis. In addition, the underlying crevice corrosion mechanism in the solution with NO_3^- is discussed.

2. Materials and Methods

2.1. Materials and Solutions

The used material was 7075-T651 (Simon Metal Materials Co., Ltd., Shanghai, China) and its composition was as follows: Zn 5.63 wt.%, Mg 2.45 wt.%, Cu 1.55 wt.%, Si 0.045 wt.%, Fe 0.18 wt.%, and Al balance. The sizes of the working electrodes used were $10 \times 10 \times 5$ mm^3 and $20 \times 10 \times 5$ mm^3. The electrode with $10 \times 10 \times 5$ mm^3 was applied for electrochemical measurements and the $20 \times 10 \times 5$ mm^3 electrode for morphology analysis. Prior to tests, the working electrodes were polished with 1500 grit silicon carbide paper, then washed with deionized water, and degreased with acetone (Sinopharm Chemical Reagent Co., Ltd., Shanghai, China). The test solution was a 3.5 wt.% NaCl solution (pH = 2), without and with different concentrations of $NaNO_3$ (0 wt.%, 0.2 wt.%, and 0.5 wt.%). All tests were performed at a temperature of 30 °C.

2.2. Configuration of Crevice and Experimental Device

Figure 1 shows the crevice structure and test setup. The crevice configuration that is shown in Figure 1a, consisting of one electrode with an exposed area of 2 cm^2, was used for morphology analysis. One half of the electrode was inside the crevice, and another half was outside the crevice. The crevice structure and test setup used for the electrochemical test, shown in Figure 1b, consisted of two identical 7075-T651 electrodes with an exposed area of 1 cm^2. One electrode (WE1) was placed inside the crevice, and another one (WE2) was located outside the crevice. A Pt/IrOx electrode was embedded in the crevice former and was used to measure the concentration of H^+ of inside the crevice. The inner counter electrode (CE1) and reference electrode (RE1) were used for the electrochemical measurements of WE1, while the outer counter electrode (CE2) and reference electrode (RE2) were used for the electrochemical measurements of WE2. A PTFE gasket with 200 μm thickness is installed between two epoxy modules to create a 200 μm crevice.

According to the protocol in reference [20], the Pt/IrOx electrodes were prepared with the following steps. First, 50 mL 1.5 g/L $IrCl_4 \cdot xH_2O$ was prepared and 0.5 mL of aqueous 30% H_2O_2 was added. Then, the solution was stirred for 10 min. Next, 0.25 g of oxalic acid ($C_2H_2O_4$) was added and the solution was stirred for another 10 min. Gradually anhydrous potassium carbonate was added to the solution until the pH was slowly raised to 10.5. The

electrodeposition process was -conducted using cyclic voltammetry (CV) scanning between 0.2 and 0.75 V (vs. Ag/AgCl) with a scanning rate of 50 mV/s for 100 cycles and then heat treatment was carried out at 100 °C for 2 h.
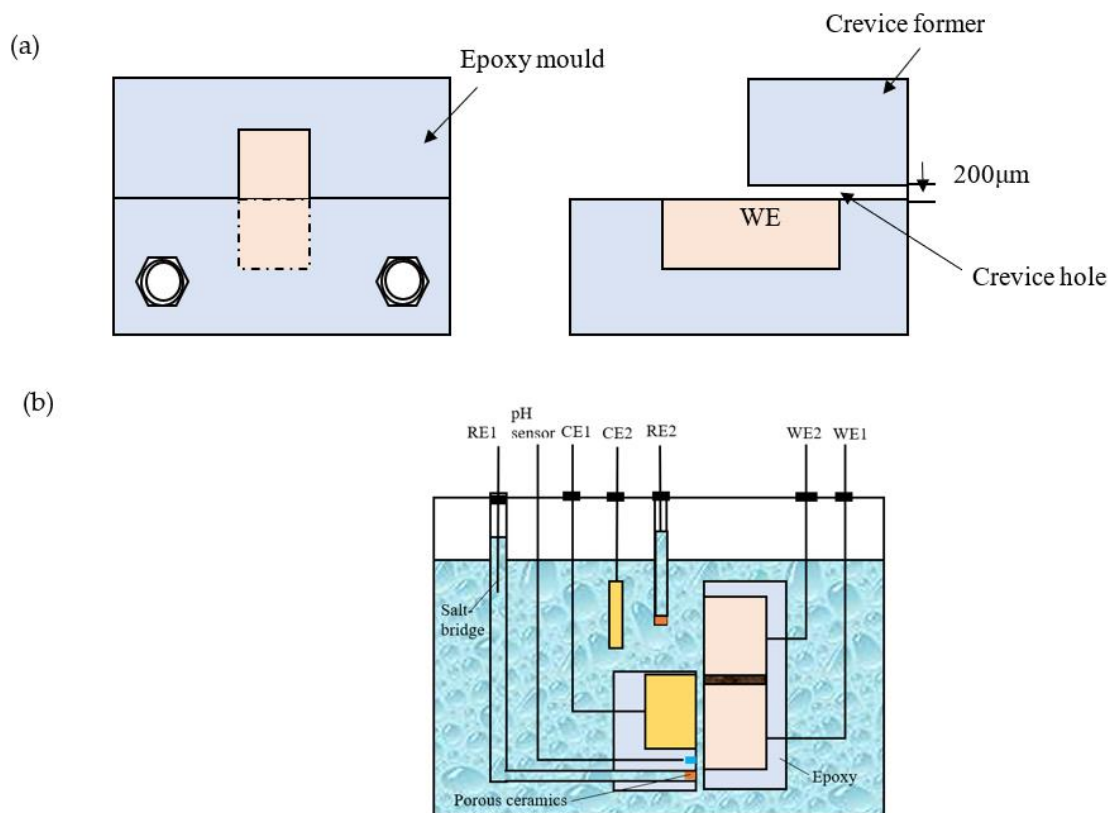

Figure 1. Configuration of the crevice and sketch map of the setup. (**a**) Crevice configuration for morphology analysis; (**b**) crevice configuration and sketch map of the setup for electrochemical tests.

The schematic diagram of the setup shown in Figure 2 was used to figure out the effect of chemical species on crevice corrosion of the 7075-T651 aluminium alloy. This setup consisted of two chambers, and each chamber contained a 7075-T651 specimen. One of the chambers was used to simulate the crevice environment, and another was used to simulate the bulk solution. These two chambers were connected by a salt bridge. The simulated bulk solution was exposed to air. However, the simulated crevice solution was purified using N_2 during the test, because the oxygen inside the crevice should be depleted due to the limited mass transfer processes by the narrow crevice opening size. These two specimens were always connected in the test.

2.3. Electrochemical Tests

A CS 330 electrochemical workstation (CorrTest, Wuhan, China) was used to explore the electrochemical corrosion behaviour of the 7075-T651 aluminium alloy. Electrochemical impedance spectroscopy (EIS) was measured over a frequency range from 100 kHz to 10 mHz using a 5 mV amplitude sinusoidal voltage. The electrochemical measurements were conducted using an electrochemical workstation. The cathodic reactions were hardly inhibited. Therefore, the potentiodynamic polarization curve of the specimen inside the crevice was recorded at a scan rate of 0.5 mV/s starting from −25 mV against open circuit potential (OCP). Correspondingly, the specimen outside the crevice was measured starting from −150 mV to 150 mV against OCP.
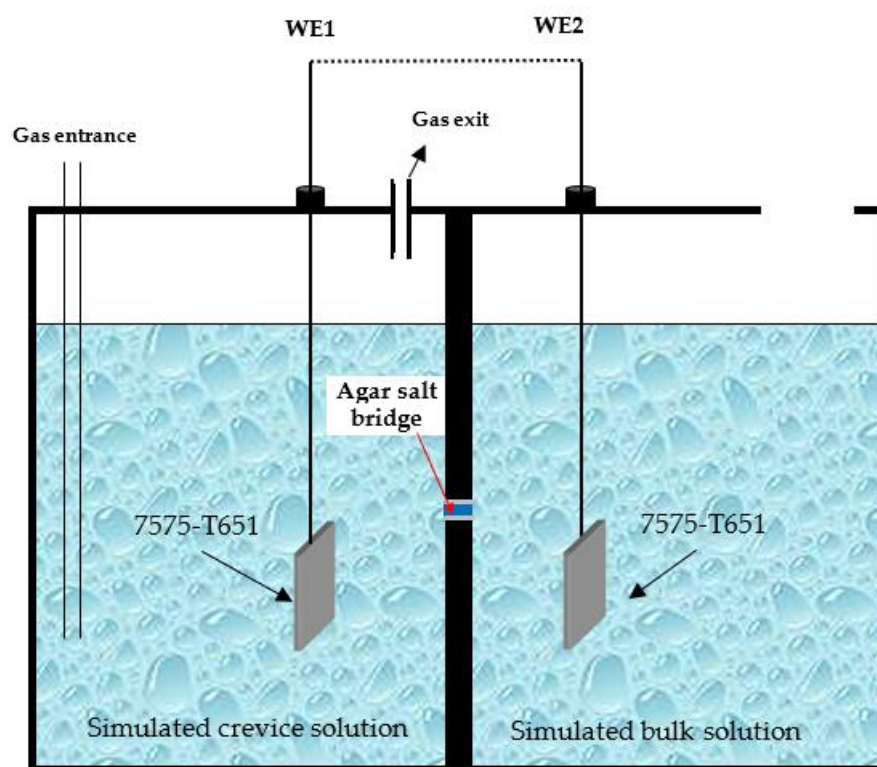
Figure 2. Schematic diagram of the two-chamber setup for corrosion morphology analysis in simulated crevice solution and bulk solution.

### 2.4. Morphology Analysis

A digital camera was used to acquire optical images of 7075-T651 after crevice corrosion. The surface microstructure and cross-sections of the crevice specimen were characterized using scanning electron microscopy (SEM). The elemental composition of the localized corrosion area inside the crevice was analysed using energy dispersive spectroscopy (EDS). The 3D morphology of the specimens after removing the corrosion products was detected using a 3D ultra-depth microscope.

3. Results

3.1. OCP Tests

Figure 3 exhibits the OCP of the specimen inside and outside the crevice in solution with various contents of $NaNO_3$. It can be seen that the OCPs outside the crevice are always more positive than those of specimens inside crevice. This is mainly attributed to the inhibited cathodic reactions inside crevice. The OCPs of the specimens outside the crevice initially shift in the positive direction and reach relatively stable values in the solutions with various concentrations of $NaNO_3$. Then, a significant potential difference between the alloy inside and outside the crevice is formed in the different test solutions. The alloy inside the crevice acts as anode and the alloy outside crevice works as cathode. However, the OCPs of the specimens inside the crevice show different evolution tendencies in the solutions with different concentrations of $NaNO_3$. In the solution without $NaNO_3$, the OCPs move to the negative direction within 4 h of immersion; then shift to the positive direction and reach relatively stable values after immersion for 8 h. However, in the solutions with $NaNO_3$, the OCPs move to the positive direction within 4 h of immersion, then shifts to the negative direction, and reach relatively stable values after immersion for 11 h. It has been acknowledged that the corrosion potential is determined by cathodic and anodic reaction kinetic processes [21–23]. The cathodic reactions inside the crevice are inhibited due to the depleted cathodic reactants. Thus, the evolution of OCPs of the specimen inside the crevice could represent the anodic reaction kinetic behaviour of the

specimen inside the crevice. The enhanced anodic reaction results in the negative shift of OCPs; on the contrary, the OCPs move in the positive direction. This indicates that the dissolution of the aluminium alloy inside the crevice increases during the initial 4 h of immersion and is gradually inhibited after 4 h in the solution without NaNO$_3$. The OCPs of the specimen inside the crevice rapidly shift to the positive direction during 4 h of immersion in the solution with NaNO$_3$, indicating an inhibited anodic reaction rate. This can be attributed to the promotion of passive film growth on the specimen surface by NO$_3^-$ inside the crevice in a solution containing NaNO$_3$. The negative displacement of OCPs suggests an enhanced dissolution of the specimen inside the crevice after 4 h of immersion, which can be related to the degradation of the passive film inside the crevice.
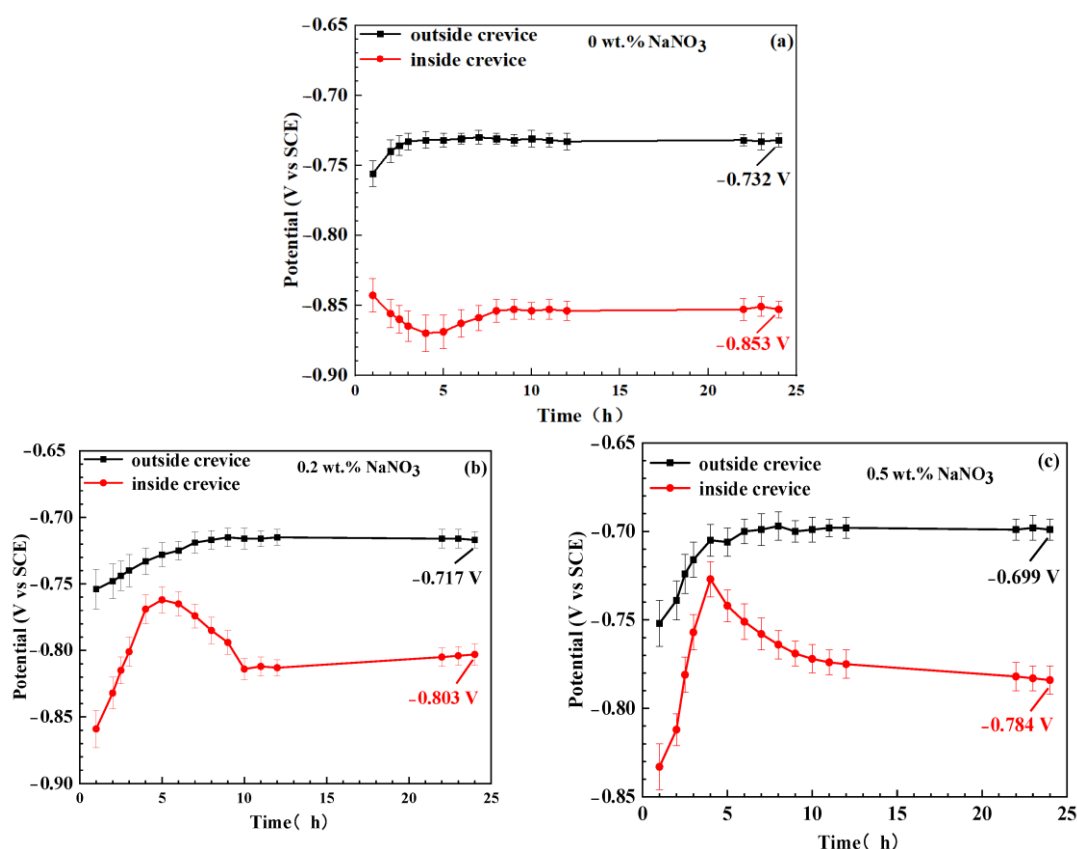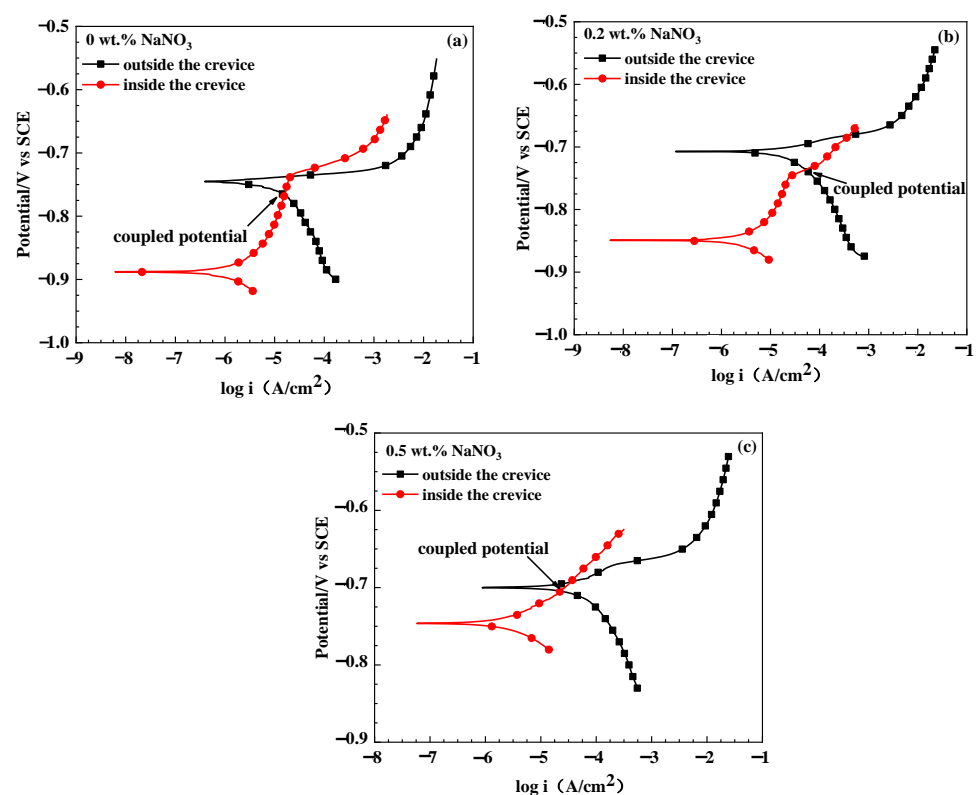

Figure 3. The OCPs of specimens inside and outside the crevice in solutions with different concentrations of NaNO$_3$ after corrosion for 24 h. (**a**) 0 wt.% NaNO$_3$, (**b**) 0.2 wt.% NaNO$_3$, (**c**) 0.5 wt.% NaNO$_3$.

3.2. Potentiodynamic Polarization Curve Tests

Figure 4 shows the polarization curves of WE1 and WE2 in the solutions with different concentrations of NaNO$_3$ after 24 h of immersion. In the solution without NaNO$_3$, the polarization curve of WE1 shows passive–active transition characteristics. This implies the passive film of WE1 is stable at corrosion potentials ranging from −0.895 V to −0.738 V. However, WE2 shows active corrosion characteristics, indicating that the passive film on the surface of WE2 was broken after 24 h of immersion. Furthermore, it can be seen that the coupled potential (the potential at the intersection of the anodic polarization curve of WE1 and the cathodic polarization curve of WE2) lies in the passive region (−0.895 V~−0.738 V) of the polarization curve of WE1. This indicates that the passive film of WE1 is stable when the specimens inside and outside the crevice are coupled together. Thus, 7075-T651 is not susceptible to crevice corrosion in the solution without NaNO$_3$ after 24 h of immersion. In the solution with 0.2 wt.% NaNO$_3$, it can be seen from Figure 4b that the passive film of WE1 is stable at a potential range from −0.848 V to −0.748 V. The stable potential range of the passive film is narrower in the solution with 0.2 wt.% NaNO$_3$ than in the solution

without NaNO$_3$. Furthermore, the current density (at -0.82 V) of WE1 is about 28 μA in the solution without NaNO$_3$ and 77 μA in the solution with 0.2 wt.% NaNO$_3$. This indicates the performance of the passive film inside the crevice becomes poorer in the solution with 0.2 wt.% NaNO$_3$ than it is in the solution without NaNO$_3$ after 24 h of immersion. Moreover, it can be seen from Figure 4b that the coupled potential exceeds the pitting corrosion breakdown potential of the passive film of WE1. Thus, the passive film inside the crevice can be broken when WE1 and WE2 are connected. This means that 7075-T651 is susceptible to crevice corrosion in the solution with 0.2 wt.% NaNO$_3$ after 24 h of immersion. In the solution with 0.5 wt.% NaNO$_3$, the anodic current density of WE1 increases rapidly with increased anodic polarized potential. This indicates that the passive film on the specimen inside the crevice was broken, initiating its susceptibility to crevice corrosion in the solution with 0.5 wt.% NaNO$_3$ after 24 h of immersion. Thus, it can be concluded from Figure 4a–c that NaNO$_3$ significantly promotes the corrosion of 7075-T651 inside the crevice.

Figure 4. The polarization curves of specimens inside and outside the crevice in solutions with different concentrations of NaNO$_3$ after corrosion for 24 h. (**a**) 0 wt.% NaNO$_3$, (**b**) 0.2 wt.% NaNO$_3$, (**c**) 0.5 wt.% NaNO$_3$.

3.3. EIS Tests

The EIS plots of WE1 and WE2 in the solutions with different concentrations of NaNO$_3$ after 24 h of immersion are shown in Figure 5. The corresponding equivalent circuits and interfacial structures between substrate and solution are shown in Figure 6. It can be observed in Figure 5a, that the impedance spectrum of WE1 contains two capacitance loops in the solution without NaNO$_3$, where the capacitance loop at high frequencies can be ascribed to the oxide film. In contrast, the capacitance loop at low frequencies can be attributed to the double layer. Then, the interfacial structure of WE1/solution and the equivalent circuit are shown in Figure 6a. The impedance spectrum of WE2 is characterized by two capacitance loops and an inductance loop at low frequencies in the solution without NaNO$_3$, as shown in Figure 5a. The inductance loop at low frequencies is related to localized corrosion of the aluminium alloy [24,25]. The two capacitance loops

result from the oxide film and the charge transfer process. Then, the interfacial structure of WE2 in solution and the equivalent circuit are shown in Figure 6a in the solution without NaNO₃. The impedance spectra of WE1 and WE2 contain two capacitance loops and an inductance loop in the solution with 0.2 wt.% NaNO₃, which is similar to that of WE2 in the solution without NaNO₃. This indicates that localized corrosion can be initiated on both WE1 and WE2. However, the diameter of the capacitance of WE1 is smaller than that of WE2 in the solution with 0.2 wt.% NaNO₃, suggesting the occurrence of crevice corrosion. The interfacial structure of WE1(WE2) in solution and the equivalent circuits are shown in Figure 6b. The impedance spectrum of WE1 contains two capacitance loops and an inductance loop in the solution with 0.5 wt.% NaNO₃. This indicates the occurrence of localized corrosion of the specimen inside the crevice. The impedance spectrum of WE2 consists of two capacitance loops similar to that of WE1 in the solution without NaNO₃, indicating an oxide film covers on the specimen surface. The interfacial structures of WE1(WE2) in solution and equivalent circuits are shown in Figure 6c. The fitted results are listed in Table 1. It can be observed that the Rp of WE2 is smaller than that of WE1 in the solution without NaNO₃. However, the Rp of WE2 is larger than that of WE1 in the solution with NaNO₃. This demonstrates that crevice corrosion can be initiated in the solution with NaNO₃ and could not occur without NaNO₃ after 24 h of immersion. Furthermore, the Rp of WE1 decreases, and the Rp of WE2 increases with an increased concentration of NaNO₃. This indicates increased corrosion of the specimen inside the crevice and inhibited corrosion of the specimen outside the crevice as the concentration of NaNO₃ increases.

Table 1. The fitted electrochemical parameters for EIS of 7075-T651 inside the crevice and outside the crevice in acidic NaCl solutions with different concentrations of NaNO₃.

| C_{NaNO_3} (wt.%)		Rs (Ω cm²)	CPE_{ox} (Ω^{-1} cm⁻² s⁻ⁿ¹)	n1	R_{ox} (Ω cm²)	CPE_{ct} (Ω^{-1} cm⁻² s⁻ⁿ²)	n2	R_{ct} (Ω cm²)	L (H/cm²)	R_L (Ω cm²)	R_P (Ω cm²)
0	Out	7.51	2.84×10^{-5}	1	32.58	3.44×10^{-5}	0.84	436.3	637.8	1570	374
	In	1.77	1.75×10^{-5}	0.89	2889	0.0189	1	3226			6115
0.2	Out	6.88	4.32×10^{-5}	0.96	964	5.80×10^{-5}	0.88	255	445	1025	1168
	In	2.13	2.81×10^{-5}	0.85	926	8.05×10^{-5}	0.78	11.43	264.5	858	937.07
0.5	Out	7.62	9.51×10^{-5}	0.84	990.3	0.039	1	706.5			1696.8
	In	2.35	4.95×10^{-5}	0.75	677.2	2.02×10^{-5}	0.86	36.61	233.2	337.6	710.00

3.4. pH Concentration Measurement

Figure 7 shows the evolution of the pH inside the crevice in the different test solutions. It can be observed that the pH shows different values inside the crevice in solutions with different concentrations of NaNO₃. The pH quickly increased from 2 to about 5.1 and gradually stabilized there. The increase in pH could be attributed to hydrogen evolution inside the crevice, which reduces the concentration of H⁺ inside the crevice. The solution inside the crevice become less aggressive than that outside crevice. Thus, the passive film could be stable inside the crevice and contribute to large corrosion resistance in the solution without NaNO₃, as shown in Figures 4–6. In the solution with NaNO₃, the pH inside the crevice increased in the first 4 h of immersion and then gradually decreased. The pH inside the crevice in the solution with NaNO₃ was lower than that without NaNO₃ after corrosion for 24 h. It could be attributed to initiation of crevice corrosion in the solutions with NaNO₃.

3.5. Corrosion Morphology Analysis

Figure 8 shows the optical and SEM images of 7075-T651 in solutions with various concentrations of NaNO₃ after crevice corrosion for 24 h. In the solution without NaNO₃, the 7075-T651 inside the crevice exhibits slight corrosion, while the 7075-T651 outside the crevice exhibits severe corrosion. This means no active crevice corrosion of 7075-T651 occurred in the solution without NaNO₃ after 24 h of immersion. In the solution with 0.2 wt.% NaNO₃, pitting corrosion is detected on the inner and outer specimen surfaces,

as shown in Figure 8b. The alloy around the pitting corrosion was hardly attacked on the specimen surface outside the crevice. However, the aluminium alloy around the pitting corrosion gradually began to corrode. Many pitting holes with different depths can be observed on the specimen surface inside the crevice. This could be attributed to the deterioration of the crevice environment, which decreased the stability of the passive film inside the crevice. The specimen outside the crevice maintained its metallic lustre and hardly suffered from corrosion in the solution with 0.5 wt.% $NaNO_3$. However, the specimen inside the crevice was covered with a layer of black corrosion product, and severe localized corrosion was observed from the optical and SEM images, as shown in Figure 8c. This means severe crevice corrosion has been initiated in the solution with 0.5 wt.% $NaNO_3$ after 24 h of immersion.
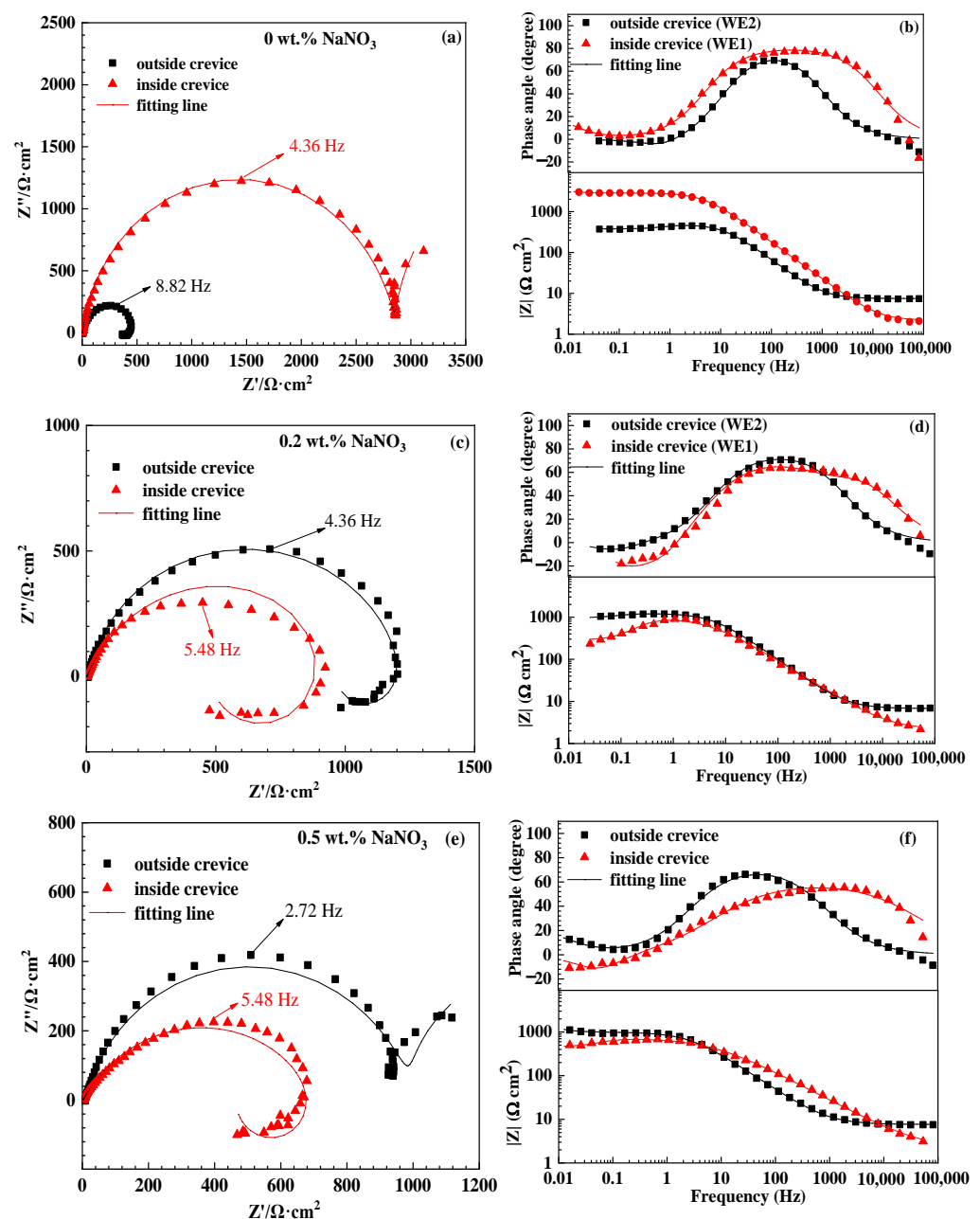
Figure 5. The EIS of specimens inside and outside the crevice in solutions with different concentrations of $NaNO_3$ after corrosion for 24 h. (**a,b**) 0 wt.% $NaNO_3$, (**c,d**) 0.2 wt.% $NaNO_3$, (**e,f**) 0.5 wt.% $NaNO_3$.
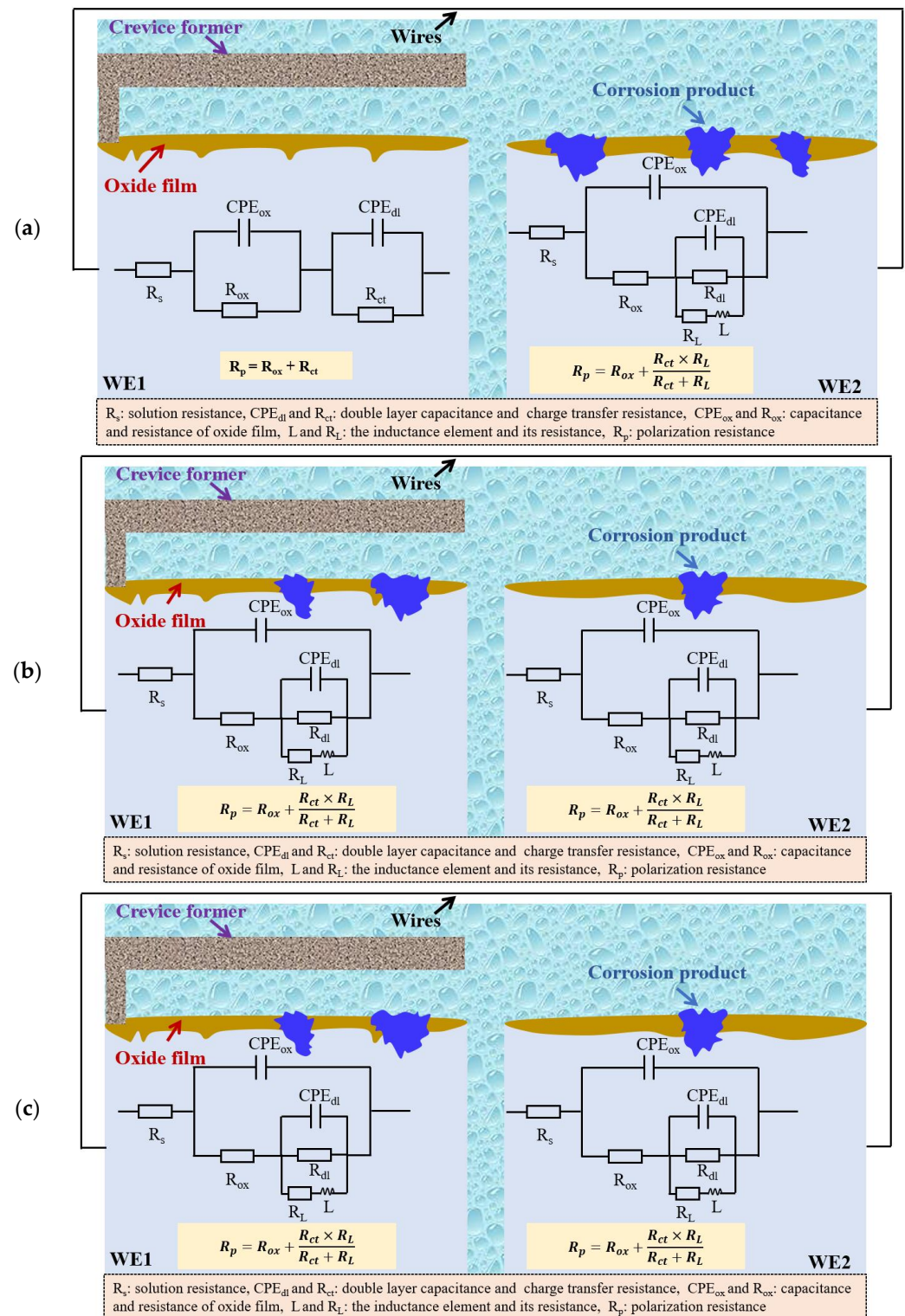
Figure 6. The interfacial structures and equivalent circuits of WE1 and WE2 specimens in solutions with different concentrations of NaNO$_3$ after corrosion for 24 h. (**a**) 0 wt.% NaNO$_3$, (**b**) 0.2 wt.% NaNO$_3$, (**c**) 0.5 wt.% NaNO$_3$.
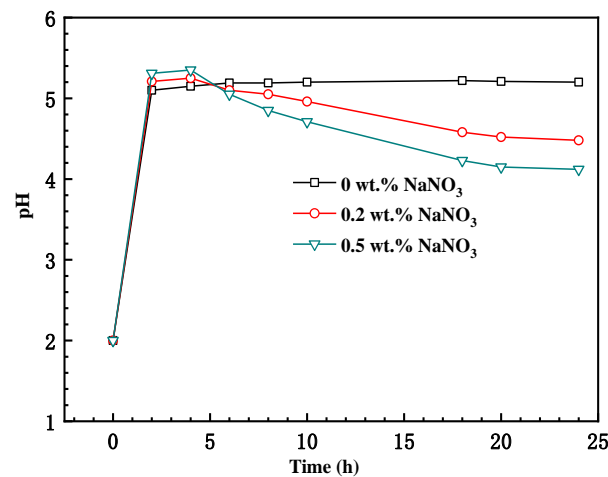
Figure 7. The evolution of the pH inside the crevice in solutions with different concentrations of NaNO$_3$.
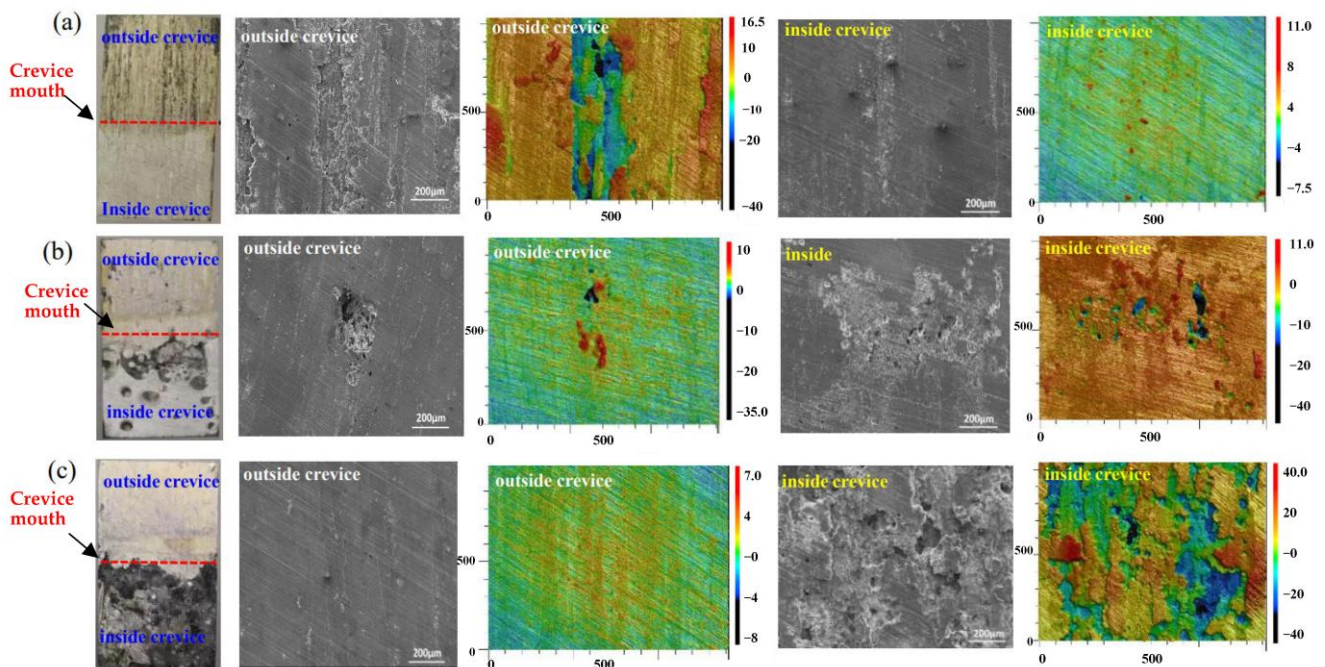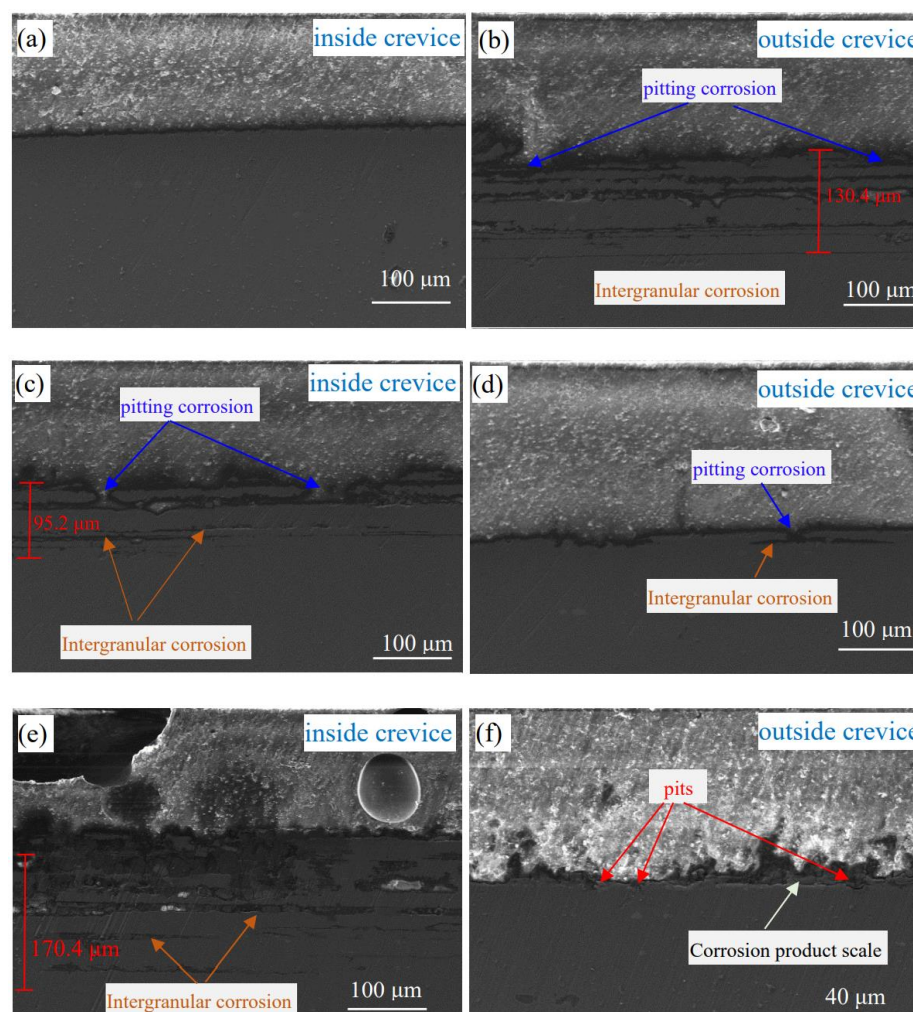

Figure 8. The macro morphology, micro morphology, and 3D depth profiles of specimens inside and outside the crevice in solutions with different concentrations of NaNO$_3$ after corrosion for 24 h. (**a**) 0 wt.% NaNO$_3$, (**b**) 0.2 wt.% NaNO$_3$, (**c**) 0.5 wt.% NaNO$_3$.

3.6. Cross-Sectional Morphology

Figure 9 shows SEM images of the cross-sectional morphology of inner and outer aluminium alloys in solutions with various concentrations of NaNO$_3$ after corrosion for 24 h. In the solution without NaNO$_3$, no apparent corrosion was detected on the aluminium alloy inside the crevice, while serious subsurface intergranular corrosion was detected on the aluminium alloy outside the crevice. The maximum depth of corroded grain boundaries attained was 130.4 μm. In the solution with 0.2 wt.% NaNO$_3$, subsurface intergranular corrosion was observed on the specimens inside and outside the crevice. However, the intergranular corrosion of the specimen inside the crevice propagated deeper and wider than that of the specimen outside the crevice, indicating the occurrence of more severe corrosion inside the crevice. Furthermore, the pitting corrosion of the grain boundaries can be observed on both inner and outer aluminium alloys. This means the pitting corrosion can induce subsurface intergranular corrosion. In the solution with 0.5 wt.% NaNO$_3$, the aluminium alloy inside the crevice suffered from severe subsurface intergranular corrosion,

and the maximum depth of corroded grain boundaries attained was 170.4 μm. However, no obvious pitting and intergranular corrosion was detected on the surface of the aluminium alloy outside the crevice. At the same time, a layer of density corrosion product scale was also observed. Furthermore, it can be seen from Figure 9a–f the corrosion of aluminium alloy inside the crevice is gradually enhanced, and the corrosion of aluminium alloy outside the crevice is progressively inhibited with an increase in $NaNO_3$ concentration. This is consistent with the electrochemical measurements. The inhibition effect on specimens outside the crevice could be ascribed to the formation of a protective oxide film with an increased concentration of $NaNO_3$. The promoted corrosion of the specimen inside the crevice by $NaNO_3$ could be related to the change in chemical species inside the crevice due to the narrow crevice openings limiting diffusion processes; however, the basic reason is unclear.


Figure 9. The cross-section of specimens inside and outside crevice in solution with different concentrations of $NaNO_3$ after corrosion for 24 h, (**a,b**) 0 wt.% $NaNO_3$, (**c,d**) 0.2 wt.% $NaNO_3$, (**e,f**) 0.5 wt.% $NaNO_3$.

3.7. The Evolution of Localized Corrosion Inside the Crevice

The evolution of localized corrosion inside the crevice was analysed using SEM and EDS to explore the effect of $NaNO_3$ on the corrosion behaviour of 7075-T651 in solutions without and with 0.5 wt.% $NaNO_3$, as shown in Figure 10. It can be seen that elemental Fe and Cu were detected at the localized corroded area after 2 h of immersion in the solution without and with 0.5 wt.% $NaNO_3$. This indicates that in the early stage, the localized corrosion inside the crevice is initiated by the intermetallic particles containing elemental Fe and Cu in the solution. However, the morphology of the localized corroded area in the solution without $NaNO_3$ was different from that in the solution with 0.5 wt.% $NaNO_3$. In

the solution without NaNO$_3$, the shallow pits were formed at the periphery of intermetallic particles, indicating that the aluminium alloy around intermetallic particles was dissolved simultaneously, perpendicular and parallel to the surface, after 2 h of immersion, as shown in Figure 10a. At an increased immersion time of 12 h, the intermetallic particles gradually detached from the aluminium alloy substrate. Some shallow pits could be observed in the solution without NaNO$_3$, as shown in Figure 10c,d. Furthermore, the bottom of these shallow pits maintained a smooth surface, indicating no further corrosion. This means that the corrosion was possibly inhibited when the intermetallic particles detached from the aluminium alloy. In the solution with 0.5 wt.% NaNO$_3$, the localized attacked area showed an irregular shape, and deep corrosion grooves or pits could be observed after 2 h of immersion. Furthermore, it could be observed that the aluminium alloy at the interface between the aluminium alloy and the localized corrosion area did not suffer from corrosion, as shown in Figure 10e. This means that the aluminium alloy around intermetallic particles tends to be corroded along the deep direction rather than the surface direction in the solution with 0.5 wt.% NaNO$_3$. At an increased immersion time of 12 h, serious localized corrosion could be observed in the solution with 0.5 wt.% NaNO$_3$, as shown in Figure 10g. Furthermore, elemental Cu and Fe could still be detected in the localized corrosion area. This indicates that the intermetallic particles still adhered to the aluminium alloy surface after 12 h immersion.
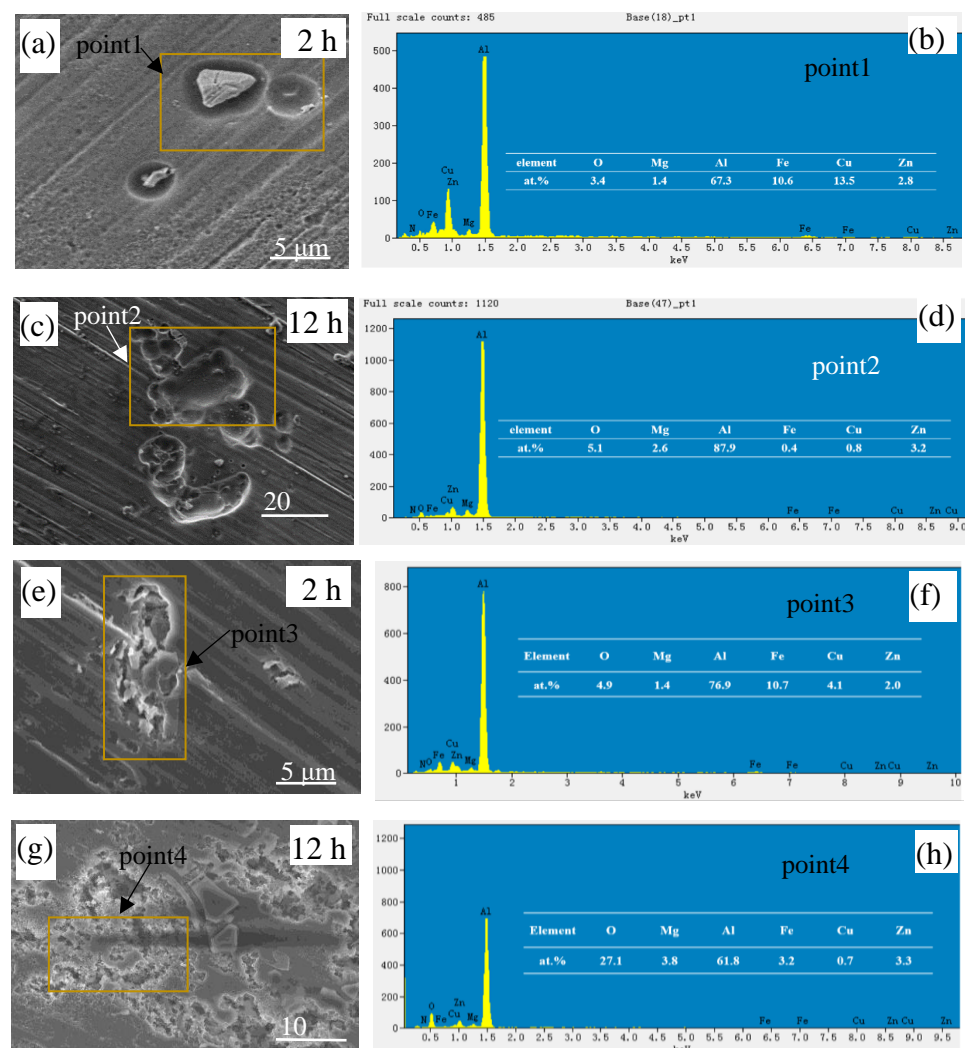
Figure 10. SEM and EDS of localized corrosion area inside the crevice in solutions without and with 0.5 wt.% NaNO$_3$ after corrosion fir 2 h and 12 h. (**a–d**) 0 wt.% NaNO$_3$, (**e–h**) 0.5 wt.% NaNO$_3$.

4. Discussion

The crevice corrosion mechanism of 7075-T651 in solution with $NaNO_3$.

According to Figure 10a,b, the localized dissolution of the aluminium alloy inside the crevice was enhanced due to the micro-galvanic corrosion induced by intermetallic particles. This resulted in a negative shift of OCPs of the specimens inside the crevice within 4 h of immersion (Figure 3a) in the acidic NaCl solution without $NaNO_3$. However, the intermetallic particles gradually detached from the specimens' surface inside the crevice at prolonged immersion time, which resulted in the disappearance of the galvanic corrosion effect, as shown in Figure 10c,d. Moreover, it can be seen from Figures 3 and 4 that the corrosion potential of 7075-T651 inside the crevice lies in the passive region of the polarization curve. Thus, an intact oxide film is formed on the specimen surface when the intermetallic particles are detached from the specimen. This inhibits the corrosion of the specimen inside the crevice and results in the positive shift of OCP of the specimen inside the crevice after 4 h of immersion (Figure 3) in an acidic NaCl solution without $NaNO_3$.
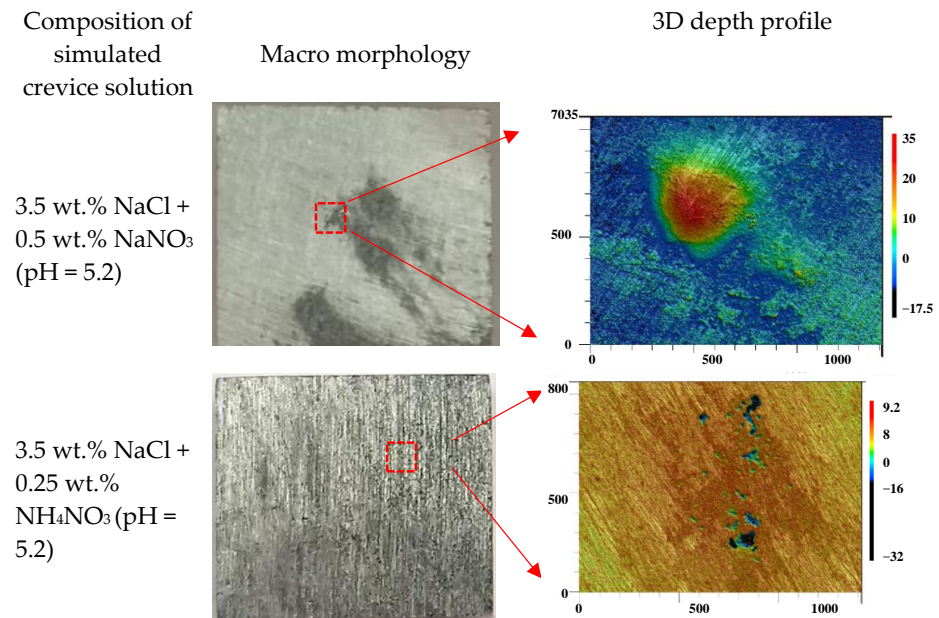
In the solution with $NaNO_3$, $NaNO_3$ plays a controversial role in the corrosion of aluminium alloys inside and outside the crevice. The $NaNO_3$ assists in the formation of a protective oxide film and reduces the corrosion of the aluminium alloy outside the crevice. At the same time, it causes severe localized corrosion of the aluminium alloy inside the crevice. Beyond all doubt, the change in chemical species inside the crevice is mainly responsible for initiating localized corrosion in solution with $NaNO_3$.

Furthermore, it has been reported [19] that NO_3^- could participate in the cathodic reactions and eventually be reduced to NH_3. This leads to the accumulation of NH_3 inside the crevice hole in the solution with $NaNO_3$. This demonstrates that the NH_3 is a potential factor in initiating crevice corrosion of 7075-T651. Thus, an experiment was performed to determine the effect of NH_3 on the crevice corrosion of 7075-T651, and the test setup is shown in Figure 2. In order to minimize the effect of the pH, the pH of all simulated crevice solutions was adjusted to 5.2 as depicted in Figure 7. As a result, two kinds of simulated crevice solutions were prepared, which were the 3.5 wt.% NaCl + 0.5 wt.% $NaNO_3$ solution with pH = 5 and the 3.5 wt.% NaCl + 0.25 wt.% NH_4NO_3 solution with pH = 5, respectively. The simulated bulk solution was the 3.5 wt.% NaCl + 0.5 wt.% $NaNO_3$ solution with pH = 2.

Figure 11 shows the corrosion morphology after 24 h of immersion. It can be seen that only a bulge point could be observed, and no obvious pitting corrosion was detected on the specimen surface in the simulated crevice solution containing 0.5 wt.% $NaNO_3$. However, obvious pitting corrosion could be detected on the specimen surface in the simulated crevice solution containing 0.25 wt.% NH_4NO_3. This indicates the presence of NH_4^+ could promote the nucleation of pitting corrosion of 7075-T651. Thus, it can be deduced that the accumulation of NH_3 inside the crevice due to the reduction of NO_3^- is mainly responsible for initiating crevice corrosion of 7075-T651. Figure 12 describes the crevice corrosion mechanism of 7075-T651 in an acidic NaCl solution with $NaNO_3$. The NO_3^- promotes the formation of an oxide film on the 7075-T651 surface, which inhibits the galvanic corrosion between intermetallic particles and the aluminium alloy, as shown in Figure 12a. This leads to a positive shift of the corrosion potential of the specimen inside the crevice at the early stage, as shown in Figure 3b,c. As the corrosion progresses, NH_3 gradually accumulates at the crevice hole due to the reduction of NO_3^-. It has been reported that NH_3 and Cu^{2+} form stable complexes $Cu(NH3)_2^{2+}$ in solution [19,26]. This suggests that the Cu of intermetallic particles is selectively dissolved by accumulated NH_3 inside the crevice, which contributes to forming irregular corrosion morphology, as shown in Figure 10e. The aluminium alloy at the interface between intermetallic particles and aluminium alloy substrate is initially exposed to a crevice solution followed by micro-galvanic corrosion due to the dissolution of Cu. However, the exposed aluminium alloy could be re-passivated at the early stage. As the corrosion progresses, the process of exposure and re-passivation of the aluminium alloy could be repeated. This generates deep corrosion grooves or pits at the interface between the intermetallic particles and the aluminium alloy substrate, as

shown in Figures 10e and 12b. With the increased depth of corrosion grooves or pits, the transportation of chemical species could be limited and result in the accumulation of metal ions inside the grooves or pits. Then, the H^+ and Cl^- inside the grooves or pits are enriched, resulting in a hydrolysis reaction and electric neutrality.

| Composition of simulated crevice solution	Macro morphology	3D depth profile
3.5 wt.% NaCl + 0.5 wt.% NaNO₃ (pH = 5.2)		
3.5 wt.% NaCl + 0.25 wt.% NH₄NO₃ (pH = 5.2)		

Figure 11. The macro morphology and 3D depth profiles of specimens in simulated crevice solution after corrosion for 24 h.

Moreover, it is difficult for NO_3^- to diffuse into the bottom of the deep grooves or pits. Thus, with the deterioration of the environment inside the deep grooves or pits, the localized corrosion is gradually stabilized. The metal ions inside the localized pits gradually migrate to the crevice solution, resulting in an increased concentration of H^+ and Cl^- in the crevice solution near localized corrosion pits. Subsequently, the passive film near the localized pits is preferentially destroyed, as shown in Figures 8 and 12c. Furthermore, according to previous reports [27–29], Cu is usually absent at the grain boundary, and this chemical heterogeneity results in high corrosion activity at the grain boundary. Thus, the exposed grain boundary is preferentially corroded, leading to serious subsurface intergranular corrosion, as shown in Figures 9 and 12c.
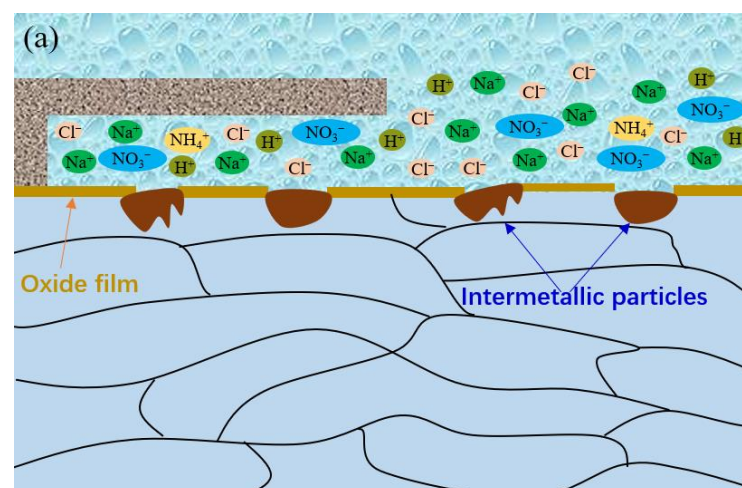
Figure 12. *Cont.*
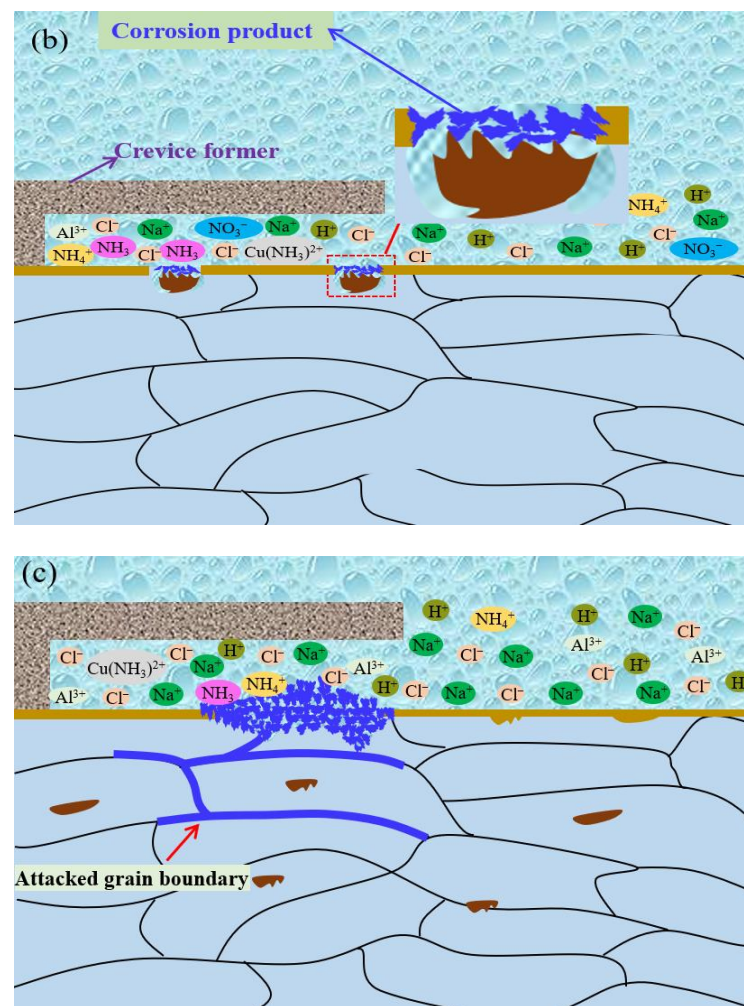
Figure 12. The crevice corrosion mechanism of the 7075-T651 aluminium alloy in acidic NaCl with NaNO$_3$, (**a**) the induction period, (**b**) the quick development period, (**c**) the stable development period.

5. Conclusions

1. NO$_3^-$ plays a crucial role in the crevice corrosion of 7075-T651. Crevice corrosion occurs in acidic NaCl solution with NO$_3^-$ and does not occur in acidic NaCl solution without NaNO$_3$.
2. The corrosion of the specimen inside the crevice is promoted, and the corrosion of the specimen outside the crevice is inhibited due to increased NO$_3^-$ concentration.
3. The secondary product, NH$_3$, induces pitting nucleation inside the crevice and then initiates crevice corrosion due to the reduction of NO$_3^-$.

Author Contributions: S.W.: Investigation, Writing—original draft. Y.C.: Investigation, Methodology, Visualization. X.L.: Methodology, Investigation, Data curation. G.C.: Supervision, Writing—review & editing. All authors have read and agreed to the published version of the manuscript.

Institutional Review Board Statement: Not applicable.

Informed Consent Statement: Not applicable.

Data Availability Statement: The data that support the findings of this study are available on request from the corresponding author.

Conflicts of Interest: The authors declare no conflict of interest.

References

1. Liu, X.; Li, Y.; Lei, L.; Wang, X. The effect of nitrate on the corrosion behavior of 7075-T651 aluminum alloy in the acidic NaCl solution. *Mater. Corros.* **2021**, *72*, 1478–1487. [CrossRef]
2. Luo, C.; Albu, S.P.; Zhou, X.; Sun, Z.; Zhang, X.; Tang, Z.; Thompson, G.E. Continuous and discontinuous localized corrosion of a 2xxx aluminium–copper–lithium alloy in sodium chloride solution. *J. Alloys Compd.* **2016**, *658*, 61–70. [CrossRef]
3. Niu, P.L.; Li, W.Y.; Li, N.; Xu, Y.X.; Chen, D.L. Exfoliation corrosion of friction stir welded dissimilar 2024-to-7075 aluminum alloys. *Mater. Charact.* **2019**, *147*, 93–100. [CrossRef]
4. Ju, H.; Liu, S.; Zhang, W.; Yang, Y.; Duan, J. Investigation of pitting corrosion and hydrogen evolution of aluminum and AA2024 alloy by simultaneous electrochemical measurements and imaging. *Electrochem. Commun.* **2021**, *132*, 107135. [CrossRef]
5. Li, Y.Z.; Wang, X.; Zhang, G.A. Corrosion behaviour of 13Cr stainless steel under stress and crevice in 3.5 wt.% NaCl solution. *Corros. Sci.* **2020**, *163*, 108290. [CrossRef]
6. Nagarajan, S.; Rajendran, N. Crevice corrosion behaviour of superaustenitic stainless steels: Dynamic electrochemical impedance spectroscopy and atomic force microscopy studies. *Corros. Sci.* **2009**, *51*, 217–224. [CrossRef]
7. Nishimoto, M.; Ogawa, J.; Muto, I.; Sugawara, Y.; Hara, N. Simultaneous visualization of pH and Cl− distributions inside the crevice of stainless steel. *Corros. Sci.* **2016**, *106*, 298–302. [CrossRef]
8. Zhu, L.Y.; Cui, Z.Y.; Cui, H.Z.; Wang, X.; Li, Y.Z. The effect of applied stress on the crevice corrosion of 304 stainless steel in 3.5 wt% NaCl solution. *Corros. Sci.* **2022**, *196*, 110039. [CrossRef]
9. Li, Y.; Mu, J.; Cui, Z.; Wang, X. The crevice corrosion behavior of N80 carbon steel in acidic NaCl solution: The effect of O_2. *Mater. Corros.* **2022**, *73*, 281–290. [CrossRef]
10. Zhang, X.; Wang, S.; Wang, X.; Cui, Z.; Cui, H.; Li, Y. The stress corrosion cracking behavior of N80 carbon steel under a crevice in an acidic solution containing different concentrations of NaCl. *Corros. Sci.* **2023**, *216*, 111068. [CrossRef]
11. Mu, J.; Li, Y.Z.; Wang, X. Crevice corrosion behavior of X70 steel in NaCl solution with different pH. *Corros. Sci.* **2021**, *182*, 109310. [CrossRef]
12. Kadri, Y.; Srasra, E.; Bekri-Abbes, I.; Herrasti, P. Facile and eco-friendly synthesis of polyaniline/ZnO composites for corrosion protection of AA-2024 aluminium alloy. *J. Electroanal. Chem.* **2021**, *893*, 115335. [CrossRef]
13. Na, K.-H.; Pyun, S.-I. Effect of sulphate and molybdate ions on pitting corrosion of aluminium by using electrochemical noise analysis. *J. Electroanal. Chem.* **2006**, *596*, 7–12. [CrossRef]
14. Udunwa, D.I.; Onukwuli, O.D.; Anadebe, V.C. Synthesis and evaluation of 1-butyl-3-methylimidazolium chloride based ionic liquid for acid corrosion inhibition of aluminum alloy: Empirical, DFT/MD-simulation and RSM modeling. *J. Mol. Liq.* **2022**, *364*, 120019. [CrossRef]
15. Li, S.; Church, B.C. Effects of sulfate and nitrate anions on aluminum corrosion in slightly alkaline solution. *Appl. Surf. Sci.* **2018**, *440*, 861–872. [CrossRef]
16. Carneiro, J.; Tedim, J.; Fernandes, S.C.M.; Freire, C.S.R.; Silvestre, A.J.D.; Gandini, A.; Ferreira, M.G.S.; Zheludkevich, M.L. Chitosan-based self-healing protective coatings doped with cerium nitrate for corrosion protection of aluminum alloy 2024. *Prog. Org. Coat.* **2012**, *75*, 8–13. [CrossRef]
17. Gao, M.H.; Zhang, S.D.; Yang, B.J.; Qiu, S.; Wang, H.W.; Wang, J.Q. Prominent inhibition efficiency of sodium nitrate to corrosion of Al-based amorphous alloy. *Appl. Surf. Sci.* **2020**, *530*, 147211. [CrossRef]
18. Balaskas, A.C.; Curioni, M.; Thompson, G.E. Evaluation of Inhibitor Performance by Electrochemical Methods: Comparative Study of Nitrate Salts on AA 2024-T3. *J. Electrochem. Soc.* **2014**, *161*, C389–C394. [CrossRef]
19. Blanc, C.; Gastaud, S.p.; Mankowski, G. Mechanistic Studies of the Corrosion of 2024 Aluminum Alloy in Nitrate Solutions. *J. Electrochem. Soc.* **2003**, *150*, B396. [CrossRef]
20. Zhu, Z.; Liu, X.; Ye, Z.; Zhang, J.; Cao, F.; Zhang, J. A fabrication of iridium oxide film pH micro-sensor on Pt ultramicroelectrode and its application on in-situ pH distribution of 316L stainless steel corrosion at open circuit potential. *Sens. Actuators B Chem.* **2018**, *255*, 1974–1982. [CrossRef]
21. Liu, B.; Zhang, X.; Zhou, X.; Hashimoto, T.; Wang, J. The corrosion behaviour of machined AA7150-T651 aluminium alloy. *Corros. Sci.* **2017**, *126*, 265–271. [CrossRef]
22. Huang, J.-l.; Li, J.-f.; Liu, D.-y.; Zhang, R.-f.; Chen, Y.-l.; Zhang, X.-h.; Ma, P.-c.; Gupta, R.K.; Birbilis, N. Correlation of intergranular corrosion behaviour with microstructure in Al-Cu-Li alloy. *Corros. Sci.* **2018**, *139*, 215–226. [CrossRef]
23. Meng, K.; Guo, K.; Yu, Q.; Miao, D.; Yao, C.; Wang, Q.; Wang, T. Effect of annealing temperature on the microstructure and corrosion behavior of Ti-6Al-3Nb-2Zr-1Mo alloy in hydrochloric acid solution. *Corros. Sci.* **2021**, *183*, 109320. [CrossRef]
24. Wang, L.; Liang, J.; Li, H.; Cheng, L.; Cui, Z. Quantitative study of the corrosion evolution and stress corrosion cracking of high strength aluminum alloys in solution and thin electrolyte layer containing Cl. *Corros. Sci.* **2021**, *178*, 109076. [CrossRef]
25. Moreto, J.A.; Marino, C.E.B.; Bose Filho, W.W.; Rocha, L.A.; Fernandes, J.C.S. SVET, SKP and EIS study of the corrosion behaviour of high strength Al and Al–Li alloys used in aircraft fabrication. *Corros. Sci.* **2014**, *84*, 30–41. [CrossRef]
26. McIntyre, J.F.; Dow, T.S. Intergranular Corrosion Behavior of Aluminum Alloys Exposed to Artificial Seawater in the Presence of Nitrate Anion. *Corrosion* **1992**, *48*, 309–319. [CrossRef]

27.   Svenningsen, G.; Larsen, M.H.; Nordlien, J.H.; Nisancioglu, K. Effect of thermomechanical history on intergranular corrosion of extruded AlMgSi(Cu) model alloy. *Corros. Sci.* **2006**, *48*, 3969–3987. [CrossRef]

28.   Svenningsen, G.; Lein, J.E.; Bjørgum, A.; Nordlien, J.H.; Yu, Y.; Nisancioglu, K. Effect of low copper content and heat treatment on intergranular corrosion of model AlMgSi alloys. *Corros. Sci.* **2006**, *48*, 226–242. [CrossRef]

29.   Lacroix, L.c.; Ressier, L.; Blanc, C.; Mankowski, G. Combination of AFM, SKPFM, and SIMS to Study the Corrosion Behavior of S-phase particles in AA2024-T351. *J. Electrochem. Soc.* **2008**, *155*, C131. [CrossRef]